Science of the Total Environment 796 (2021) 148950

Contents lists available at ScienceDirect

Science of the Total Environment

journal homepage: www.elsevier.com/locate/scitotenv

Long-term variation of boundary layer height and possible contribution factors: A global analysis

Yarong Li [a], Jiming Li [a,*], Yuxin Zhao [a], Miao Lei [a], Yang Zhao [a], Bida Jian [a], Min Zhang [b], Jianping Huang [a]

[a] Key Laboratory for Semi-Arid Climate Change of the Ministry of Education, College of Atmospheric Sciences, Lanzhou University, Lanzhou, Gansu, China
[b] Inner Mongolia Institute of Meteorological Sciences, Hohhot, Inner Mongolia, China

HIGHLIGHTS

- Quantified meteorological influences on long-term variation and trend of BLH
- Wind speed dominates long-term variation, followed by low tropospheric stability.
- Low tropospheric stability dominates the increased BLH.
- Decrease in wind speed explained 40% of decreased BLH.

GRAPHICAL ABSTRACT

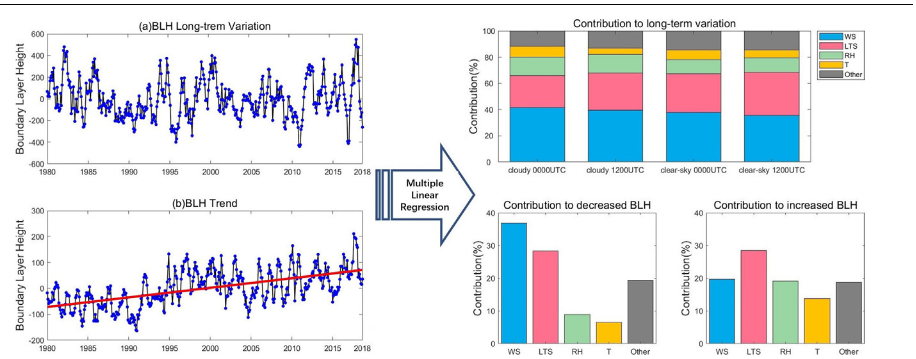

ARTICLE INFO

Article history:
Received 26 April 2021
Received in revised form 15 June 2021
Accepted 6 July 2021
Available online 10 July 2021

Editor: Anastasia Paschalidou

Keywords:
Radiosonde
Trend
Meteorological influence
Land type
Cloud

ABSTRACT

Boundary layer height (BLH) plays an important role in regulating global weather/climate, as well as the dispersion and transportation of pollutants. Until now, however, the attribution and contributions of different controlling factors to BLH long-term variability and trends have not been quantified on a global scale. The long-term radiosonde dataset was used in this study to retrieve global BLH climatology; seasonal, diurnal, long-term variation and trends were analyzed over a 39-year period (1980–2018). Statistical results show that the global distribution of the BLH and its trend have apparent day-night differences. BLH during daytime is deeper during clear-sky conditions compared to cloudy sky conditions, indicating a significant effect of clouds; BLH during nighttime is deeper under cloudy conditions. BLH was also found to vary over different land types; dry and hot soil exhibits a deeper BLH than those of wet and cool soil. The long-term variation and trend of BLH are highly influenced by near-surface meteorological parameters. In particular, based on multiple linear stepwise regression models and the contribution calculation method, this investigation initiatively quantifies the influences of meteorological parameters on global BLH long-term variation and trend. Our results emphasized that a 10 m wind speed (WS) and low tropospheric stability (LTS) have significant contributions to long-term BLH variation; WS and LTS anomalies alternately dominated the contribution of the diurnal cycle of the BLH anomaly. Annual BLH recorded an average increasing trend (38.9–42.1 m/decade), and LTS is more dominant than WS from a contribution perspective, especially for increased BLH anomaly. Contributions from near-surface temperature (T) and relative humidity (RH) also play important roles. However, a decreasing WS trend dominated the decreased trends of BLH anomaly, accounting for nearly 40% of the total contribution.

* Corresponding author.
E-mail address: lijiming@lzu.edu.cn (J. Li).

https://doi.org/10.1016/j.scitotenv.2021.148950

1. Introduction

The atmosphere boundary layer (ABL) is located at the bottom of the troposphere, encapsulating nearly all human life and industrial activities (Stull, 1988). Due to its influence on the exchanges of momentum, heat, moisture and material between the surface and the atmosphere, the ABL plays a key role in the hydrology cycle and environmental processes (e.g., agriculture, air pollution, hydrology and aviation) (Huang et al., 2020; Stull, 1988; Garratt, 1994). As a key ABL parameter, the boundary layer height (BLH) indicates the degree of vertical mixing and exchange (Seibert et al., 2000; Seidel et al., 2010), having an important impact on weather forecast and climate predictions (Seidel et al., 2010; Yim et al., 2019). In addition, the BLH determines the volume of diffusion for pollutants (Kim et al., 2007; Miao et al., 2021; Zhang et al., 2012). Its effect in regulating pollution emissions and elimination has also received wide attention over the last few decades (Ding et al., 2017; Hu et al., 2014; Miao and Liu, 2019; Zhao et al., 2019; Zhang et al., 2006). However, it is difficult to accurately simulate BLH and its variation in models (Medeiros et al., 2011; Seidel et al., 2012), because it refers to numerous physical processes considered in the parameterization scheme of the ABL, especially small-scale exchange processes occurring in the ABL (Fekih and Mohamed, 2019; Wyant et al., 2010; Garratt, 1994). Therefore, studying the BLH and its long-term variations, especially the factors that control BLH changes, is crucial to improve our understanding of air pollution and related boundary-layer processes.

As radiosonde can provide dynamic and thermal profiles within the ABL, it is considered a powerful tool for BLH measurement (Seidel et al., 2010). Currently, global radiosonde observation projects have produced long-term global records of temperature, humidity and wind profiles, which have been widely used to explore boundary layer characteristics over different regions, such as in the Arctic (Zhang and Seidel, 2011), Europe and America (Seidel et al., 2012; Zhang et al., 2013), China (Guo et al., 2016) and Japan (Zhang and Li, 2019). Many studies have been undertaken to expand our understanding of basic features of the BLH. For example, based on intensive radiosonde observations, Liang and Liu (2010) found that radiosonde-based BLH over land and oceans shows a strong diurnal cycle due to the diurnal variation of solar energy. Seidel et al. (2012) studied diurnal and seasonal BLH variations over Europe and America, recording different BLH seasonal patterns for the daytime and nighttime. In addition, the BLH at most sounding stations also exhibited significant trends over the past few decades (Zhang et al., 2013), and the BLH trend regime over China has been shown to have an abrupt shift; trends before and after 2004 recorded opposite results (Guo et al., 2019). In fact, due to the ABL being strongly affected by surface forcing (e.g., increased surface friction can reduce wind velocity, heat and water vapor fluxes may change boundary layer conditions (Stull, 1988)), diurnal and seasonal BLH cycles and its variation are therefore closely controlled by surface parameters (e.g., soil moisture (SM)) and near-surface meteorological conditions (e.g., temperature and relative humidity) (Guo et al., 2019; Zhang et al., 2018). Based on temporal correlation analysis between the BLH and meteorological variables, Guo et al. (2016, 2019) reported the BLH to be closely related to T, WS, LTS, near-surface pressure, RH and SM. Likewise, Pal and Haeffelin (2015) proposed a physical insight about how geophysical variables (e.g., solar short-wave radiation, sensible heat flux (SH), SM, T and RH) influence the BLH maximum annual cycle. In addition, the influencing mechanism of meteorological factors on the BLH has also been explored (Pal and Haeffelin, 2015; Yi et al., 2001). Bianco et al. (2011) found that irrigated fields and urban areas have a shallower BLH than areas of parched grass during an arid summer in the California Valley (USA) due to a larger part of surface net radiant flux being converted into latent heat flux (LH). Recently, Zhang et al. (2018) indicated that the BLH is higher over bare land in northwest China than wet land in southern China due to a higher surface sensible heat flux (SH) and lower near-surface RH. However, the majority of meteorological variables have inherent seasonal and daily cycles, thus correlations between them may be controlled by their strong seasonal variations which cannot fully explain BLH long-term variations. In addition, correlations between BLH and related variables (such as T, surface pressure and 500 hPa geopotential height) also vary over time and space, with opposite correlations being recorded during the day and night (Seidel et al., 2012). In addition, global climatological conditions have recently undergone significant changes (Davy and Esau, 2016; Rummukainen, 2013); its influences on the variability of the BLH have received less attention and are still poorly understood. Therefore, systematic studies about statistical relationships between long-term BLH variations and different contributory variables on a global scale should be undertaken, and relative contributions of different meteorological and surface parameters to long-term BLH variation should also be further quantified.

In order to increase our understanding of related physical processes in the ABL, and to improve parameterized schemes of BLH in models, we retrieved the BLH from the global sounding network and investigated its climatological characteristics. In particular, by combining multiple datasets, we focused on two key questions: (1) what are the factors driving long-term variation of BLH at regional and global scales? And (2) which factor has the dominant contribution? Although some statistical results agree reasonably well with previous studies, new insights are also presented. The rest of the paper consists of the following sections. Section 2 introduces data and methods. The mean climate state, long-term trends, BLH differences over different land covers, and the attribution and contribution analysis are presented in Section 3. Finally, Section 4 presents the conclusion.

2. Dataset and methodology

2.1. Radiosonde dataset

The radiosonde datasets, derived from the University of Wyoming website (http://weather.uwyo.edu/upperair/sounding.html), cover long-term radiosonde observations of 660 global stations over a 39-year period (1980 to 2018). Soundings were launched at two fixed times (0000UTC, 1200UTC), providing abundant profiles for pressure, temperature, humidity, potential temperature and wind. Although vertical resolutions of global radiosonde have significantly improved recently, the majority of stations in Asia still have poor resolution. Radiosonde networks in the southern Hemisphere and Africa have a sparse distribution, having shorter sampling periods (Fig. S1). For a better comparability and consistency of retrieved BLH, only stations with data spanning more than 20 years were taken into account; stations with periods of long-term missing data or a geographical location that has changed were removed. In this study, therefore, 488 stations at 0000UTC and 436 stations at 1200UTC met our strict conditions.

Before retrieving BLH, a series of strict quality-control procedures were performed to filter unsuitable data (Durre et al., 2006; Fig. S2). A basic parameter check was undertaken to ensure that parameters were within a reasonable range. A surface altitude inspection was undertaken to check station altitude change over a long time series; a station with an altitude difference >50 m was eliminated. An internal consistency check mainly ensured reasonable relationships existed between the pressure level and geopotential height, eliminating observations with more than one surface layer in a sounding. The repetitive data check ensured observations undertaken in both temporal and vertical directions were suitable; temporal running check considered observations showing the same data at 15 consecutive observations or 15 consecutive same time observations (e.g., 0000 UTC) to be inaccurate; vertical running check considered the same observations at five consecutive vertical layers as false observations. Similar to Seidel et al. (2012) and Zhang et al. (2013), two additional restrictions were used before calculating the BLH: (1) within 5 km above the ground, there were at least seven vertical levels of sounding records of specific humidity, virtual potential temperature, geopotential height and at least four records of wind observation; (2) at least 50 observations per season were obtained. In addition, the dewpoint depression (ΔT_d) threshold method was adopted to identify whether boundary layer clouds existed during sounding periods, and cloud layer was confirmed when dewpoint depression fell below the set threshold (Poore et al., 1995). The reference threshold was set as: if the temperature of an observed layer > 0 °C, $\Delta T_d = 1.7$ °C; if temperature ranged from −20 °C to 0 °C, $\Delta T_d = 3.4$ °C; and if the temperature < −20 °C, $\Delta T_d = 5.2$ °C. In this study, all analyses are undertaken with respect to cloudy or clear sky conditions.

2.2. Land cover and meteorological reanalysis datasets

In order to estimate BLH and its long-term change tendency over different land types, yearly updated global land cover maps (1992– 2015) were generated using data from the European Space Agency (ESA) Climate Change Initiative (CCI) and subsequent products released by Copernicus Climate Change Service (C3S). Both data sources are in good continuity and consistent with each other; data was integrated at https://www.esa-landcover-cci.org/?q=node/197. The spatial resolution of this data attained 0.00278°. The fine-resolution allowed the landscape to be described in great detail. As land cover maps from 1992 onwards were available, we only analyzed BLH properties over different land covers during this period. Analysis indicated that landscapes of 78 sounding stations had changed during this period, of which 73 of these stations had become "urban" due to urbanization; only one or two stations changed into bare land, forest or grassland. The remained 558 stations did not record a land-use change.

In addition, SH, LH, SM, soil temperature (ST), solar radiation (RS), downward thermal radiation (RT) and WS from the ERA5-Land reanalysis dataset were also used in this study. Compared with prior versions of ECMWF global climate reanalysis, the latest fifth-generation ERA5-Land reanalysis dataset has considerable improvement and its temporal resolution had been increased to include an hourly level; horizontal spatial resolution was $0.1° \times 0.1°$. In addition, simultaneous T and RH profiles were obtained from radiosonde data. LTS is expressed as:

$$\Delta\theta = \theta_{700} - \theta_s \tag{1}$$

where, θ is potential temperature; and $_{700}$ and s indicate 700 hPa and the surface. All meteorological variables used in this study can fundamentally reveal the thermodynamic and dynamic conditions of the ground and near-surface atmosphere. Thermal characteristic variables (SH, LH, RS, RT, ST and T) reflect the energy budget in the lower atmosphere, indicating that ground heating and cooling control turbulent development (Bianco et al., 2011; Pal and Haeffelin, 2015; Pielke, 2001; Tanaka et al., 2007; Yi et al., 2001; Zhao et al., 2019). As humidity conditions (i.e., SM, SH) regulate the energy balance of the surface, net surface radiation is mainly converted into LH and SH, and surface humidity conditions can influence the distribution ratio (Banta, 2003; Meng et al., 2017), referred to as the Bowen ratio. Moreover, SM can alter surface albedo (Sanchez-Mejia and Papuga, 2014), RH is associated with surface evaporation and vegetation transpiration, and the surface water-vapor flux is also an important contribution of buoyancy flux for wet ground (Endo et al., 2008). WS alters the contribution to turbulence generated by mechanical effects, and WS also affects the ABL structure by horizontal transport (Banta, 2003). Finally, LTS indicates thermodynamic conditions in the lower atmosphere (Guo et al., 2019).

2.3. Calculation of BLH and its long-term variation

Currently, the most common methods of determining BLH based on radiosonde datasets include the parcel method (Liang and Liu, 2010), the gradient method (Wang and Wang, 2016; Seidel et al., 2010), temperature inversion layer height (Seidel et al., 2010), and the Richardson number method (Zhang et al., 2020; Zhang and Seidel, 2011). Differences, and advantages and disadvantages between these methods were reviewed by Seidel et al. (2012). It is believed that there are notable differences and uncertainties in calculating BLH using different methods, and none of the currently used methods can perfectly capture BLH. Each method has its inherent shortcomings, and they are only suitable to calculate BLH under certain conditions; it is therefore important that the adopted method should be dependent on the research subject. By using long-term radiosonde observations, Seidel et al. (2012) evaluated almost all methods, concluding that the optimal method to study BLH climatology is the widely used bulk Richardson number method (Vogelezang and Holtslag, 1996). As the physical meaning of the bulk Richardson number method is the dimensionless ratio between the suppression of turbulence produced by buoyancy and turbulence generated from wind shear, it considers both dynamic and thermodynamic effects comprehensively. This method has obvious advantages over other methods because it is suitable for both convective and stable boundary layer regimes, being valid when raw radiosonde data is under low vertical resolution (Leventidou et al., 2013). Formulation for this method is:

$$R_i(z) = \frac{(g/\theta_{vs})(\theta_{vz} - \theta_{vs})(z - z_s)}{(u_z - u_s)^2 + (v_z - v_s)^2 + bu_*^2} \tag{2}$$

where, g is gravitational acceleration; θ_v is virtual potential temperature; u and v denote wind components whose units have been converted from *knots* into *m/s*; z is height away from the ground; z and s represent variables at altitudes of z and the ground; u_* is friction velocity, and $bu_*{}^2$ is the friction term that is negligible due to a much smaller value than the other term in the denominator (Vogelezang and Holtslag, 1996). According to Stull (1988), surface turbulence exists when R_i is less than the critical value of 0.25. The corresponding bulk Richardson number R_i at each sounding level can be obtained using Eq. (2). By scanning the R_i profiles upward from the surface, in conjunction with a linear interpolation between the level with R_i initially exceeds 0.25 and the adjacent sounding level below it. BLH may therefore be determined when $R_i = 0.25$. After calculating BLH, the Mann-Kendall trend test (Kendall, 1975; Mann, 1945) and Sen's slope estimation (Sen, 1968) were used to assess linear trends of BLH and their significance tests.

In order to investigate the long-term variations of BLH and meteorological variables, and to further explore their interrelationships, seasonal cycles of these variables were removed from their monthly-mean values. By using this method, anomalies for both BLH and other variables on a monthly scale were obtained as (Pal and Haeffelin, 2015):

$$H'_k = H^k - \overline{H}^k \tag{3}$$

where, H represents the monthly mean value; k is the month; $\overline{H}^k$ represents averaged H of the kth month among 39-years; and $H_k{}'$ represents the anomaly.

After removing seasonal factors, obtained time series of variables were still non-stationary for long-term variation analysis due to the trend in the variable causing spurious covariation (Raffalovich, 1994). We therefore adopted a detrend method derived from monthly anomalies minus its least square fitted line. By using stepwise regressions, the irrelevant variables were filtered and linear linkages between the BLH anomaly and variable anomalies were established. We also conducted collinearity diagnostics on variable anomalies and no significant collinearities were found. Regression model was based on the following function (Che et al., 2019a; Jian et al., 2018):

$$\Delta H = \frac{\partial H}{\partial x_1}\Delta x_1 + \frac{\partial H}{\partial x_2}\Delta x_2 + \cdots + \frac{\partial H}{\partial x_i}\Delta x_i + c \tag{4}$$

where, all variables have undergone normalized procedure (mean = 0, standard deviation = 1). ΔH is BLH anomaly; Δx_i is the independent variable anomaly, which is reserved in a stepwise regression model when the statistical significance test is met (>90%); i is the number of variables; c is a constant term; and $\frac{\partial H}{\partial x_i}$ is the regression coefficient.

Based on the regression models in Eq. (4), we further quantified the relative contribution of each meteorological variable to BLH long-term variation. Contribution was calculated using the formulation (Huang and Yi, 1991):

$$C_i = \frac{1}{m}\sum_{j=1}^{m}\left(H_{ij}^2 / \sum_{i=1}^{n} H_{ij}^2\right) \tag{5}$$

where, m is the data length in the time series; n is the total amount of variables considered in the stepwise regression model, $H_{ij} = c_i\, x_{ij}$, in which c_i is the regression coefficient; and C_i denotes contribution rate of ith variable.

2.4. Uncertainty analyses about the method

Under strong winds or deep boundary layers, radiosondes may drift far from their launch point, causing ambiguous land classification and cloud identification. Here, as the horizonal resolution of the land type dataset was 300 m, we considered the dominant land type within 3 km of the radiosonde as the station land type. Secondly, during the radiosonde horizontal drifts, the corresponding surface parameters will also change. However, current available ERA5-land surface parameters have a the highest resolution of 10 km, indicating that the surface parameters are fixed when the sounding balloon reaches the top of the ABL. This may introduce some uncertainty in the calculation of contribution rates. Thirdly, we didn't make a clear distinction of boundary layer types (convective or stable) due to the rough vertical resolution of many radiosonde observations, especially early observations; these factors may bias averaged BLH results. Additionally, we know that the convective clouds are strongly linked to the convective boundary layer, whereas stratiform clouds may or may not be linked to the ABL. In our study, as a simple dewpoint depression threshold method cannot distinguish cloud types, we therefore only focused on BLH behavior under cloudy and cloud-less conditions.

3. Results and discussion

3.1. Global characteristics and trends

This section presents the global distribution of multi-year averaged BLH and its long-term trend, including seasonal and day-night differences. Note that the averaged BLH is derived by using the bi-weight mean estimator (Lanzante, 1996), which is more robust for BLH with non-normal distribution. Distinct day-night differences were found in the BLH due to fixed sample time, during our analysis we categorized data into two periods to clearly distinguish the daytime and nighttime ABL. For the region of 60°W–120°E, 0000 UTC encompassed 20:00–08:00 LT (the nighttime period) and 1200 UTC encompassed 08:00–20:00 LT (the daytime period).

The global distribution of multi-year averaged BLH at 0000 UTC and 1200 UTC under cloudy- and clear-sky conditions are shown in Fig. 1a–d. In general, BLH ranged from less than 200 m to nearly 2 km. High BLH appeared over Europe and Western Asia at 1200 UTC, and over the western mountains of North America at 0000 UTC (where BLH even exceeded 2 km); shallow BLH was mainly located over the Eurasia continent (0000 UTC), America and East Asia (1200 UTC), corresponding to nighttime BLH. BLH over eastern areas of China exhibited a weak day-night difference, possibly being due to the local sounding time in this

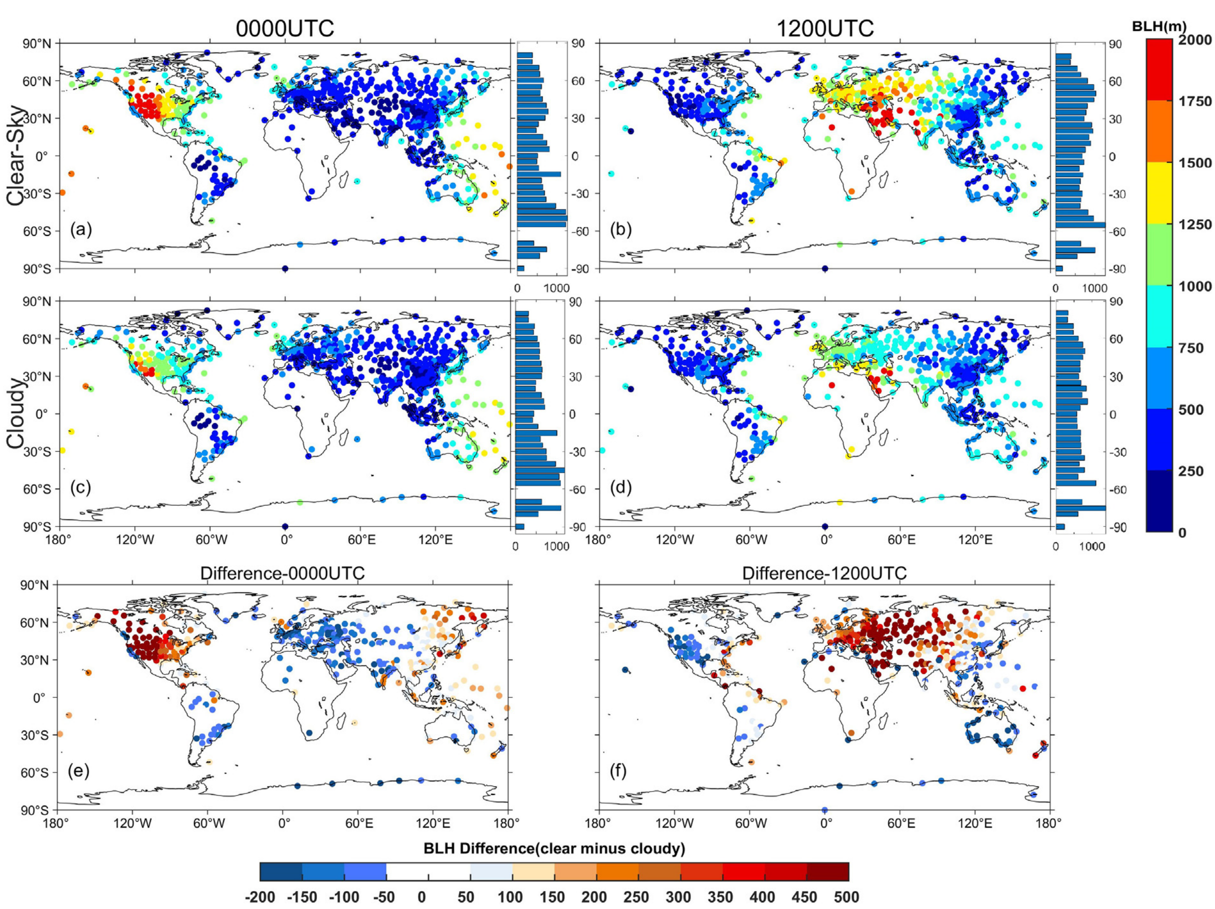

Fig. 1. (a)–(d) for the spatial distribution of multiyear averaged BLH over period 1980 to 2018, both BLH under clear sky (top) and cloudy (middle) is provided here, the left panel for 0000 UTC and the right for 1200 UTC. Only stations sampled for more than 20 years are presented in the figure. The histograms to the right of the subplots represent the zonal mean. (e), (f) for the differences between clear-sky BLH and cloudy.

area coinciding with BLH transition periods in the morning and evening, when the ABL was near-neutral and turbulence had a similar intensity (Blay-Carreras et al., 2014); day-night differences at these two periods were therefore weak.

Radiosonde at the two fixed synoptic time periods only captures two "snapshots" of the ABL structure (Seibert et al., 2000). Due to different local sampling times, BLH at the two sampling times represent obvious zonal gradient. Results indicate that the global distribution of BLH is controlled by a strong diurnal cycle, linked to the daily cycle of energy budgets for both the Earth's surface and atmosphere, and peak BLH is basically distributed in areas where sounding samples were collected in the afternoon period. For example, BLH over the western part of North America exceeds 2 km at 0000 UTC, while the lowest height is only about 120 m at 0000 UTC. In addition, spatial characteristics of BLH distribution are also related to latitude, altitude and cloud cover. For example, differences in latitude are associated to changes in the angle of the sun, where a more stable boundary layer with shallow height occurs at high latitudes (Seidel et al., 2010), with low- and mid-latitude regions recording a higher BLH due to receiving more solar energy. However, the highest BLH is not found in the tropics but in the mid-latitudes, this may be due to the fact that the tropics are mostly oceanic. Although there may be thicker BLHs in the Sahara, our dataset has few samples from these regions. In addition, the utilized bulk Richardson method is a little bit uncertain in the tropics due to frequent deep convection (Seidel et al., 2012). Elevation may be another factor related to global distributions (altitude is not shown); previous studies have recorded deep radiosonde-based BLH to exhibit dependence on stations with higher altitudes (e.g., western North America Plateau (Seidel et al., 2012) and the Tibet Plateau (Guo et al., 2016)). Guo et al. (2016), however, considered deeper BLH recorded over the Tibet Plateau to be related to strong wind speeds. The near-sea BLH may be obviously influenced by sea-land breezes (Fig. S3), during the day, sea breezes bring cold, high-humidity flows to the near-sea stations, resulting in a BLH that shallower than its adjacent continental stations (Huang et al., 2016). At night, dry land breezes generate more turbulence induced by mechanical effects, BLH of the near-sea stations therefore responds to higher levels; the diurnal cycle of near-sea BLH is therefore weaker.

Boundary layer cloud has been recorded to have a significant influence on BLH (Wang and Wang, 2014; Zhang et al., 2018). Clouds can inhibit shortwave radiation reaching the surface (Molod et al., 2015), resulting in shallower BLH during the daytime. The impact of clouds on the BLH can be clearly seen from BLH differences between clear skies and cloudy conditions (Fig. 1e–f). Clouds tend to inhibit ABL development during the daytime, especially over Siberia, Europe and North America, where clear-cloudy BLH differences may reach 500 m. During the nighttime, however, our results indicate that cloud cover may maintain a deeper BLH (Europe, western Asia and western part of North America). The nocturnal boundary layer is generally characterized with stable stratification, with sporadic turbulence existing when the surface temperature decreases to become colder than the air temperature (Stull, 1988), hence height is always considered to be the top of the surface inversion layer. During cloudless nights, downward atmospheric radiation is weak, resulting in rapid surface cooling due to heat loss; turbulent exchange is therefore greatly suppressed during this period. In contrast, longwave flux emitted by clouds can induce net heating effects (Harrison et al., 1990) during cloudy nights, thereby slowing down surface cooling, resulting in global mean BLH to be about 90 m higher than those during clear nights. However, deeper nighttime BLH under cloudy conditions persist until earlier period before sunrise, when the BLH is less affected by cloud cover (e.g., eastern Asia at 0000 UTC and eastern North America at 1200 UTC). This means that the cloud effect is insignificant during earlier periods before sunrise; other factors, such as surface non-thermal conditions (e.g., SM (Xu et al., 2021), WS (Banta, 2003)) and topped entrainment processes (Angevine, 2007) may also play more important roles.

Comparison of annual and seasonal trends of global BLH under clear sky and cloudy conditions (Fig. 2) indicated that only 280 stations (from 434 valid stations) exhibited statistically significant annual trends, with an average clear-sky (cloudy) trend of 42.1 (38.9) $m \cdot dec^{-1}$ (Fig. 2a5–d5), having the same magnitude with previous results (Zhang et al., 2013; Zhang and Li, 2019). Our results also indicate that BLH trends under clear-sky and cloudy conditions had similar distributions and values. However, trends at two observed times had opposite results, indicating that the global distribution of BLH trends was also related to different controlling factors and day-night differences. Land areas over central and western Eurasia were dominated by increased trends at 1200 UTC; at 0000 UTC trends were significantly weakened or became negative, with trends over central Eurasia becoming insignificant. Previous investigations recorded radiosonde-based BLH trends over Europe (Zhang et al., 2013) and Japan (Zhang and Li, 2019) to also have similar day-night differences. In addition, trends during the day were more strongly affected by clouds, with central and western Eurasia (1200 UTC) and North America (0000 UTC) having smaller trend values during cloudy periods.

Global mean trends for four seasons under clear-sky conditions were 60.5 (MAM), 53.5 (JJA), 46.4 (SON) and 45.3 (DJF) $m \cdot dec^{-1}$; mean trends for cloudy periods were slightly smaller (59.5, 50.0, 45.6 and 46.5 $m \cdot dec^{-1}$, respectively). Under both conditions, values decreased with the season cycle, recording higher results during MAM and lowest results during DJF (or SON). Trends recorded among the seasons were notably different, for example, the number of stations with statistically significant trends over the Eurasia continent gradually decreased from MAM to DJF, with trends in some stations (e.g., clear-sky trends in East Asia at 1200 UTC) even shifting from positive values in MAM to negative values in other seasons. This result explains why the mean trend during MAM was much higher than those recorded during the other seasons. In addition, clouds may result in some trends becoming insignificant, especially for stations during daytime periods. Under cloudy conditions, stations recording a significant trend in central Eurasia were sparse during JJA, SON and DJF; their annual mean trends were thereby distinctly lower than those under clear sky conditions.

3.2. BLH characteristics over different land types

Regional observations indicate that BLH over different land types is distinctly different due to differences in surface parameters and meteorological conditions (Friedl et al., 2010; Pielke, 2001). 78 stations with altered landscapes (due to rapid urbanization) were excluded from this analysis (Fig. S4). Here, BLH at 0000 UTC and 1200 UTC were combined to ensure enough samples were collected.

BLH values for 17 land types under cloudy- and clear-sky conditions are shown in Fig. 3. The number of stations for corresponding land types is also presented with histograms being organized (top to bottom) using mean BLH. Results indicate BLH to be generally lower under cloudy conditions than under clear-sky conditions: mean BLH ranged from 485 m (deciduous needle-leaved) to 842 m (vegetation covered flood) under cloudy, and from 486 m (lichen and moss) to 1019 m (bare land) under clear-sky conditions. The clear-cloudy differences had noticeable variations. For example, difference over lichen and moss land (3 stations) was only 6 m while deciduous needle-leaved land (4 stations) was 191 m. It should be noted that all deciduous needle-leaved stations were located in one time zone (100.23°E–113.86°E), coinciding with a larger clear-cloudy BLH difference (Fig. 1e–f). In light of this uncertainty, further analyses focused on land with more than 20 stations and with station location spanning multiple time zones (eight land types met this standard, see the red labels in Fig. 3a–b).

For eight land types, average BLH over bare land and shrubland was consistently higher; irrigated cropland consistently recorded the lowest BLH. Generally, higher BLH existed on land with low humidity, vegetation fraction and albedo; lower BLH was recorded on land with opposite

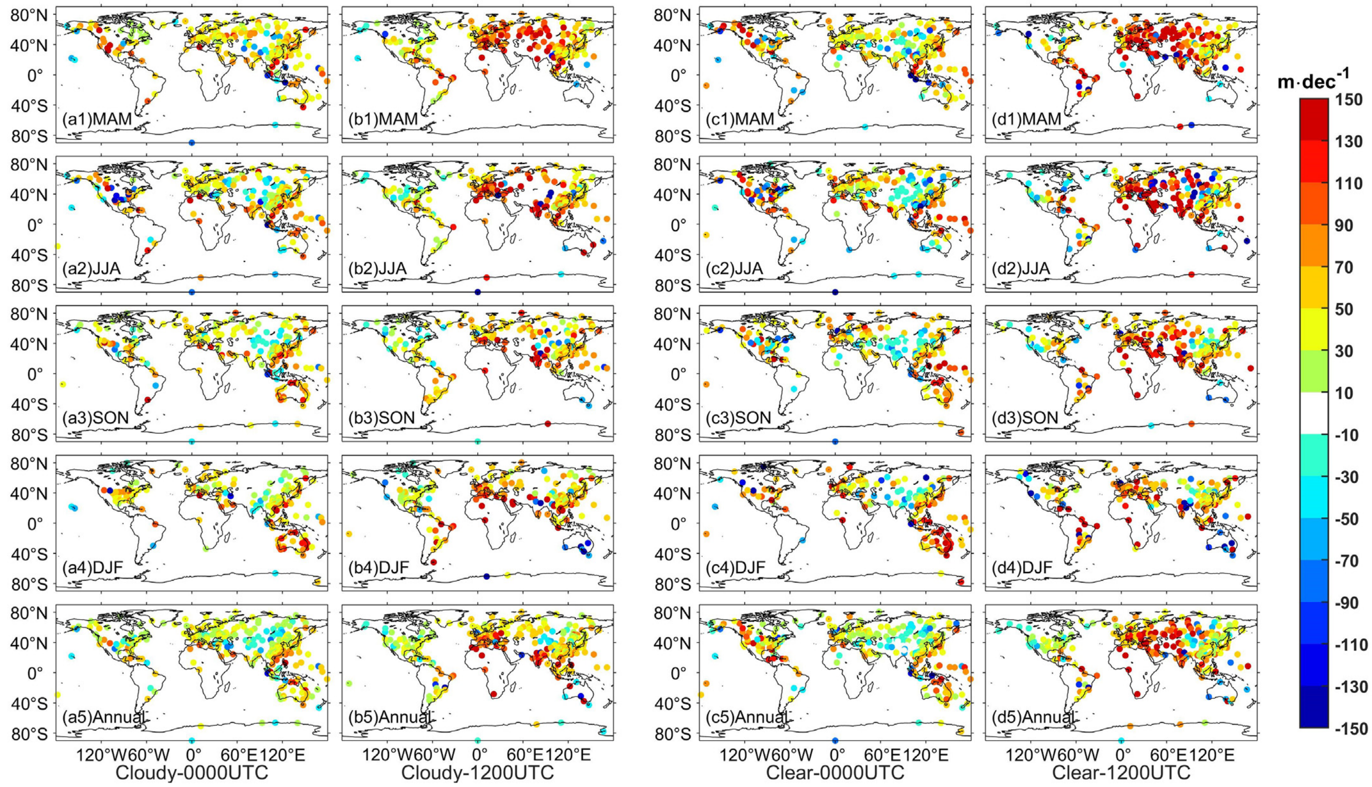

Fig. 2. Global distribution of seasonal and annual BLH trends (unit: m · dec^{-1}); trends are statistically significant ($p < 0.05$). The bottom panel presents annual trends, for the seasonal trends, MAM: March, April, May. JJA: June, July, August. SON: September, October, November. DJF: December, January, February. Left panel denotes trends under cloudy conditions at 0000UTC and 1200UTC, respectively, right panel for cases under clear sky conditions.

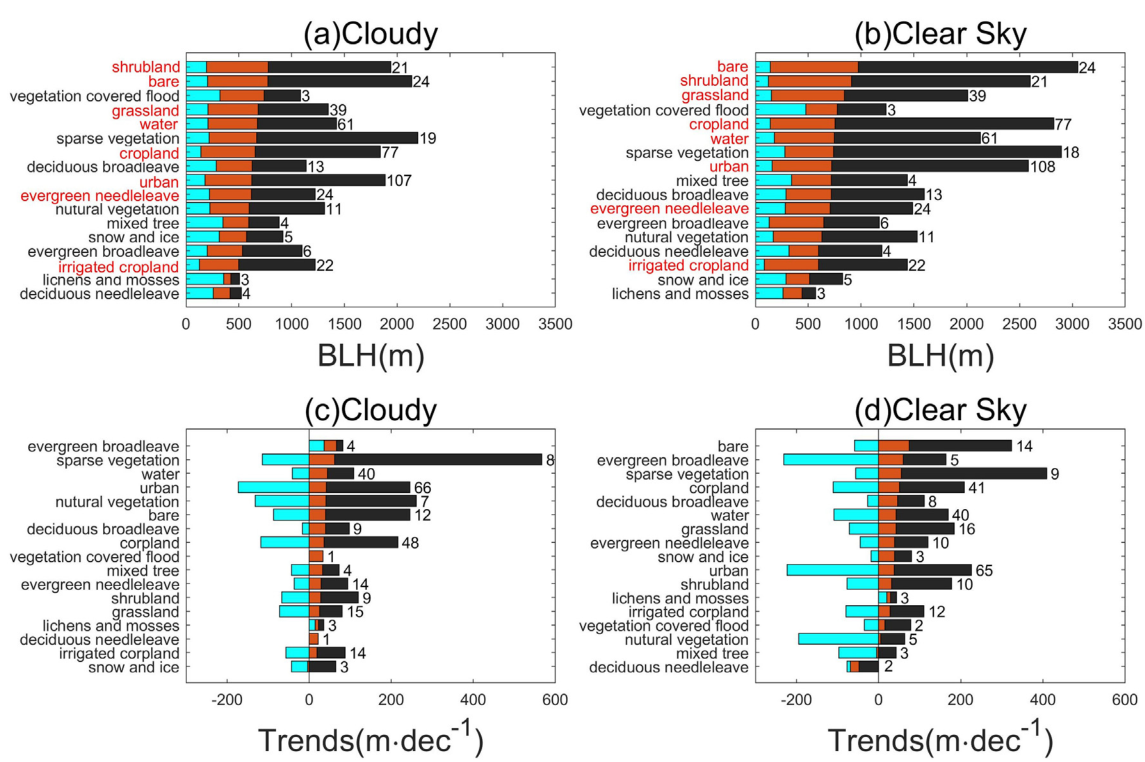

Fig. 3. (a)–(b) the cloudy and clear sky BLH over 17 land types. BLH at 0000 UTC and 1200 UTC are combined, and the histogram is organized (top to bottom) by mean BLH (orange bar); maximum (black) and minimum (cyan) values are also presented here. The number of stations is shown in right side of histogram, that number > 20 is marked as red Y-axis label. (c)–(d) the BLH trend over 17 land covers, notably, the ordinate of each sub-figure is ordered differently.

characteristics, consistent with other recent findings (Sanchez-Mejia and Papuga, 2014; Zhang et al., 2018). However, huge differences over the same land type still exist. It can be seen in Fig. 3a–b, that the higher the number of stations, the larger the BLH variation range. It has previously been shown that lower soil moisture levels or relative humidity results in more surface net radiation flux distributed to the sensible heat flux, which is conducive to the development of the ABL (Pal and Haeffelin, 2015). For areas of shrubland and bare land, relatively dry soil could be an essential cause for higher BLH; low levels of roughness correspond to high horizontal wind speeds (Wever, 2012), which contributes more to mechanical effects induced turbulence, thus being another reason for its higher BLH. Although albedo in shrubland and bare land were the highest, its impact on BLH is insignificant over these land types. Here, albedo is not the only factor determining surface parameters (e.g., temperature); soil thermal properties and solar radiation are also important aspects (Xiao and Bowker, 2020). As wet areas (e.g., water, irrigated cropland) are accompanied by high soil moisture, evaporation or transpiration, they recorded relatively shallow BLH; meteorological conditions over these lands caused more surface energy to be distributed in latent heat, therefore resulting in shallower BLH (Bianco et al., 2011). Due to evergreen needle-leaved forests being mainly distributed in cold temperate zones, low temperature and solar energy may be highly related to shallow BLH. In addition, average urban BLH was also recorded to be similar to that of evergreen needle-leaved or irrigated cropland. In fact, urban areas often have a higher surface heat flux (White et al., 1978) and higher BLH than adjacent surrounding areas due to the urban heat island effect (Pal et al., 2012). Across all land types, urban area accounted for the largest number of stations (>100), resulting in a more comprehensive and larger variation range, and more nocturnal BLH may bias the average results; furthermore, combined BLH at 0000 and 1200 UTC could also be influence to the statistics. Lower averaged BLH is therefore generally recorded in urban areas and its varying amplitude is greater than most areas.

Annual BLH trends over 17 land types are presented in Fig. 3c–d. Here, averaged values of maximum and minimum trend are provided in the histogram, with trend bars arranged by mean values from bottom to top. These results indicate that more than half of the stations over each land type had a significant trend (95% confidence level). Under cloudy conditions, mean trends ranged from $-3.6\ \mathrm{m \cdot dec^{-1}}$ (snow and ice) to $66.7\ \mathrm{m \cdot dec^{-1}}$ (sparse vegetation); under clear skies, values varied from $-68.\ 5\ \mathrm{m \cdot dec^{-1}}$ (deciduous needle-leaved) to $74.4\ \mathrm{m \cdot dec^{-1}}$ (bare land). For all land types, average BLH trends were generally positive, with only deciduous needle-leaved land recording a decreasing trend under clear skies. However, results from three stations did not represent the complete tendency state over this land type. Results for trend differences between clear and cloudy skies over the eight land types (Table S1) indicate that mean trends were reduced under cloudy conditions, apart for urban and water stations where mean trends were slightly lower under clear sky conditions. As per our previous analysis, BLH trends at one station significantly varied by day and night, or by season, thus increasing and decreasing trends coexist over the same land type and the trend range significantly varied with land cover.

In order to estimate diurnal BLH cycles over the eight land, we converted two fixed observed times into local time for each station (Fig. 4). Here, it is worth noting that the diurnal cycle in the present analysis was only formed by combining stations located at different time zones, variation in meteorological conditions (e.g., solar radiation, wind speed etc.) over different stations may introduce some uncertainties. However, our statistical results still revealed some basic features of BLH diurnal variation. Regardless of the underlying surface, BLH increased from the morning with an increase in solar radiation, reaching a daily peak around 15:00 LT (Liang and Liu, 2010; Zhao et al., 2019). Under cloud conditions, the daily peak was reached slightly earlier. Daily maximum and minimum values at each land-cover are basically consistent with BLH upper and lower limits (Fig. 3a–b), indicating that BLH differences under the same land cover type is mainly caused by diurnal variation. Other possible factors (e.g., latitude, altitude and meteorology factors) were not taken into account here. In addition, under clear skies, daily variation amplitude was larger than that under cloudy skies. As previously discussed, once clouds were present, the convective boundary layer increased more slowly during the daytime, and the nocturnal BLH was slightly higher than that under clear skies. BLH exhibits a different diurnal cycle across various land covers. For example, maximum BLH on bare land and shrub land can reach around 2500 m during the midday period under clear skies, but night minimum BLH was only 224 m. However, stations situated in water, characterized by high humidity and low diurnal temperature ranges, recorded a weak diurnal variation compared with those of other land types. Diurnal cycles of trends over eight land types (Fig. S5) have maximum and minimum values that are consistent with the distribution shown in Fig. 3c–d. As noted earlier, only a few stations recorded a decreasing trend; decreasing trends were easily identified in stations at night and increasing trends dominated daytime stations, usually reaching a peak value by midday.

3.3. Contributions from different factors to BLH variation and trend

Based on the long-term variations of related meteorological factors, the regression model of BLH anomaly at each station was established using Eq. (4). Apart for some mid-latitude stations over Asia, high-correlations (95% confidence level) between observed and model predicted time series of BLH anomalies were exhibited at most stations, indicating that the stepwise regression models have good prediction for BLH anomaly (Fig. S6). Compared with other areas, low vertical resolutions over stations in East Asia may result in uncertain retrieval of the BLH, which are partly related to poor regressions in these areas. Due to a lack of ERA5-land derived meteorological factors (RS, RT, SH, LH and WS) over a few sporadic island stations in the southwest Pacific, contribution analyses for these stations were not provided.

3.3.1. Contributions to BLH long-term variation

The contribution rates of meteorological variables to BLH long-term variation were derived using Eq. (5) (Fig. 5). Due to similar results recorded under clear and cloudy conditions, only contribution distributions under clear skies were provided (cloudy conditions are provided in Fig. S7). For the majority of stations, LTS and WS are always retained in the regression models, indicating that the variations of the two variables are closely related to BLH variation. Other variables were shown to have weak or insignificant contributions. Quantified contributions indicate that LTS and WS had the dominant contributions to BLH variations over the majority of stations; their contributions exhibited distinct spatial and day-night differences. For example, WS was the dominant factor during the night, or at high latitude areas, and the maximum contribution rate of WS exceeded 50%. However, the contribution of WS during the nighttime was insignificant at stations over central and western Asia (i.e., the Iranian plateau and its eastern regions; red box in Fig. 5j1). This was largely due to the stepwise regression failing to pass the significant test over this region (Fig. S6). In addition, the anomaly in LTS accounted for a considerable contribution of daytime stations at low and middle latitudes. Rough diurnal cycles of contribution over the eight main land types under clear sky (Fig. S8) and cloudy (Fig. S9) were calculated. It was seen that LTS contribution gradually increased during the morning while the contribution of WS declined; nighttime contribution was dominated by WS and the contribution of LTS only exceeded that of WS in the afternoon period. In summary, LTS and WS alternately dominated the daily anomaly in BLH. As previously highlighted, the influence of land surface on BLH is mainly reflected in the buoyancy flux and the mechanical shear effect (Banta, 2003; Pino and Vilà-Guerau De Arellano, 2008). During nighttime periods, the mechanical shear effect is generally the only process producing boundary layer turbulence (Stull, 1988), near-surface WS is closely related to these mechanical

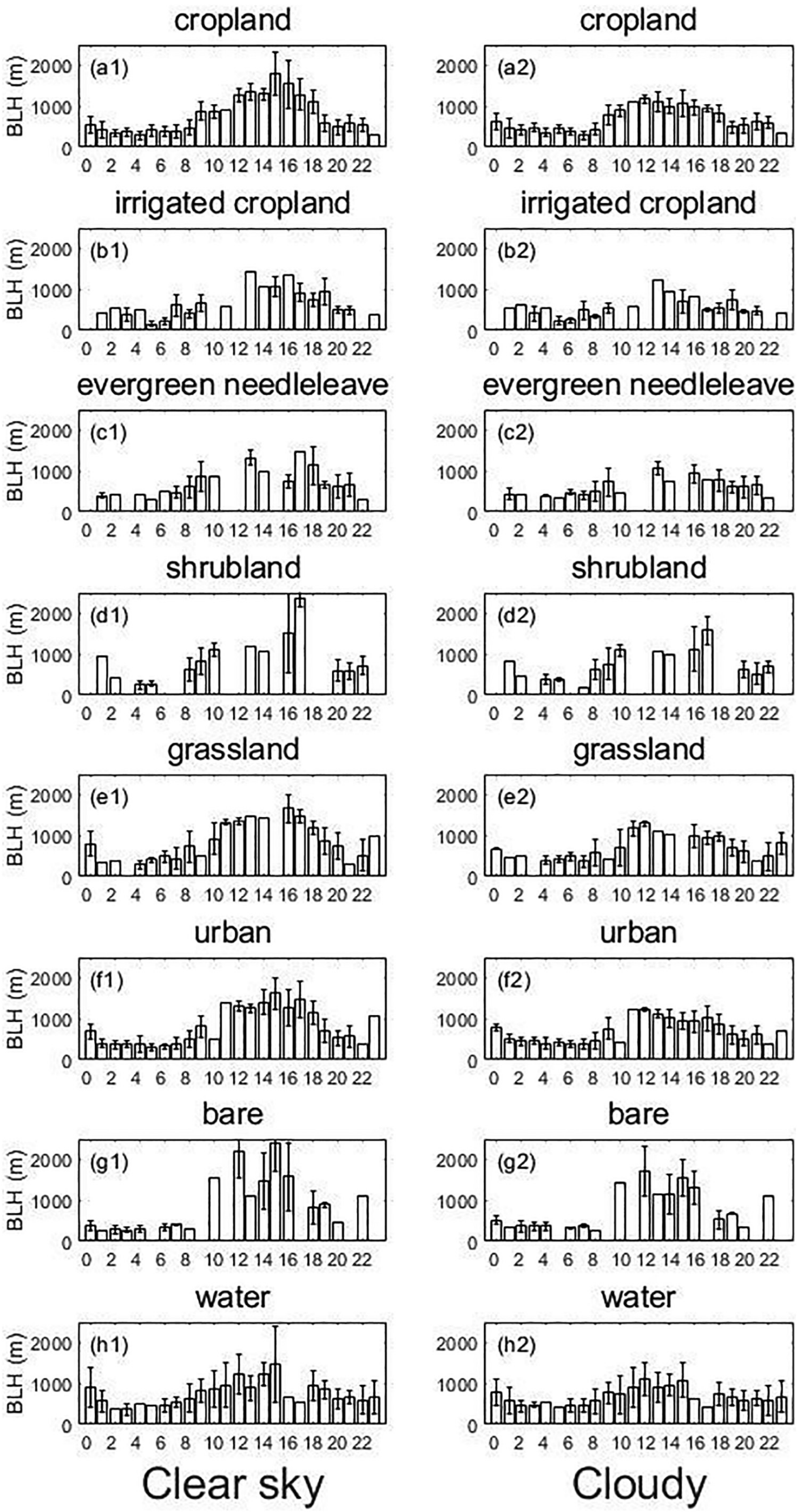
cropland
(a1)
(a2)
irrigated cropland
(b1)
(b2)
evergreen needleleave
(c1)
(c2)
shrubland
(d1)
(d2)
grassland
(e1)
(e2)
urban
(f1)
(f2)
bare
(g1)
(g2)
water
(h1)
(h2)
BLH (m)
0
1000
2000
0 2 4 6 8 10 12 14 16 18 20 22
Clear sky
Cloudy

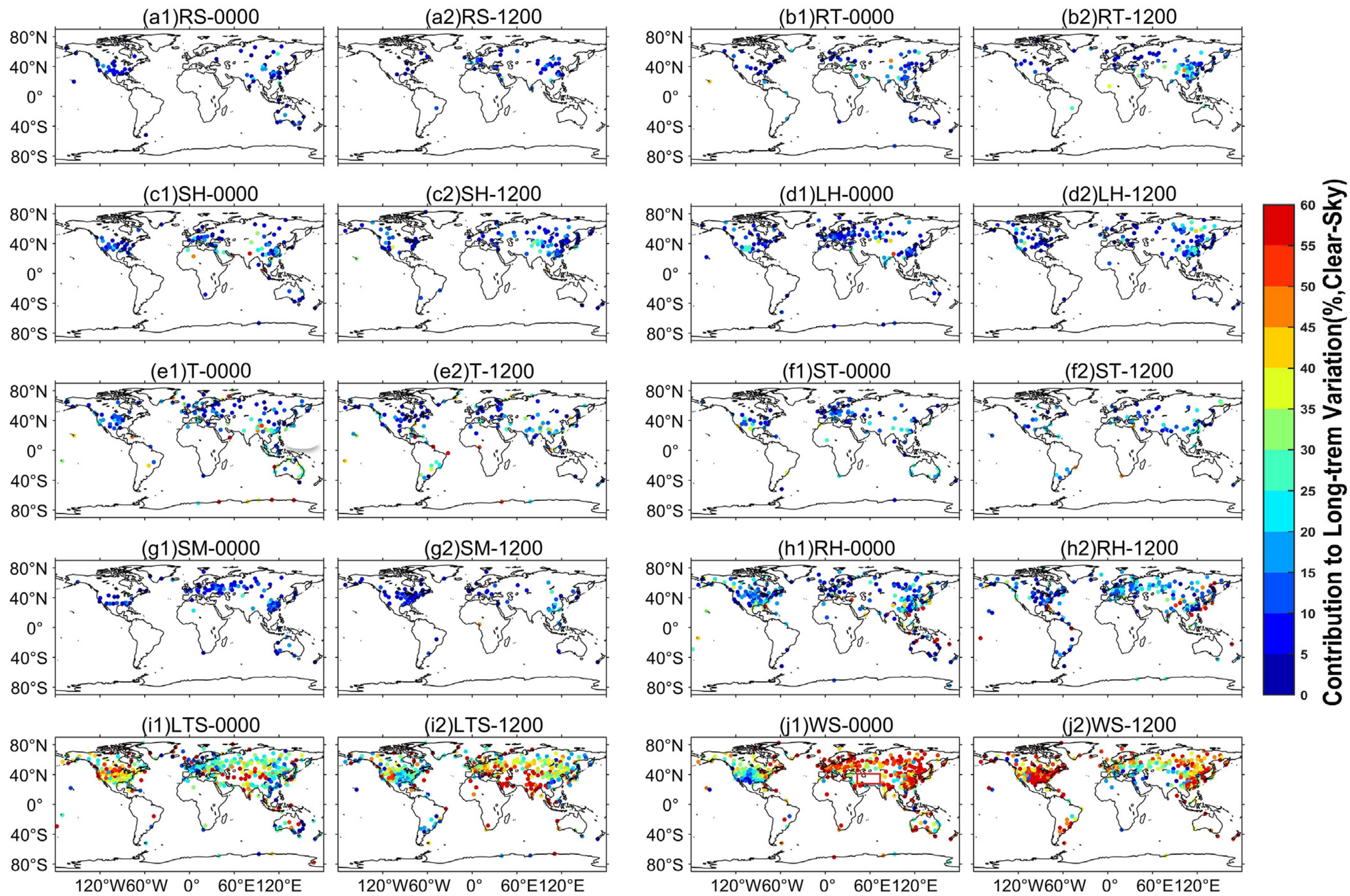

Fig. 5. The contribution rates from anomalies of meteorological variable to BLH anomaly. Here, RS: solar radiation, RT: thermal radiation, SH: sensible heat flux, LH: latent heat flux, T: near surface air temperature, ST: surface soil temperature, SM: surface soil moisture, RH: near surface relative humidity, LTS: low tropospheric stability, WS: 10 m wind speed. "0000" and "1200" represent UTC. Red box in (j1) denotes the region where the regression models did not pass the correlation test ($p < 0.05$).

effects. However, unstable-stratified ABL mainly occurs during thermal instability or during convection conditions produced by strong surface heating during daytime periods (Garratt, 1994); these unstable conditions can induce variation in LTS. The contribution of the mechanical shear effect during the daytime is therefore not as great as that at night; the contribution of cloudy LTS anomaly is essentially lower than those under clear skies due to more vigorous instability, whereas WS and RH contributions under cloudy conditions to be slightly increased (compare to Fig. S7). Although RS, RT, T, ST, SH, LH, RH and SM, which reveal energy and water vapor supply related to buoyancy flux, play important roles in driving ABL growth, anomalies of these factors over long-term periods do not indicate significant contributions to the long-term variation of BLH in many cases their anomalies were eliminated by regression models.

It is worth noting that we selected anomalies instead of raw values to build the regression model, thereby already removing trends and seasonal cycles. However, if we only take original series of observed values into account, BLH and other variables exhibit significant correlations. As shown in Fig. S10, BLH is negatively correlated with RH and LTS, and positively correlated with WS and LH. This is consistent with the prior findings (Guo et al., 2019; Pal and Haeffelin, 2015; Zhang et al., 2018; Zhang et al., 2013). Correlation coefficients of other parameters (SH, T, ST, RT, RS and SM) with BLH exhibited obvious day-night differences; contrary correlation coefficients between daytime and nighttime were highlighted in Fig. S10; similar findings were also recorded by Seidel et al. (2012). This possibly indicates that the driving mechanisms to ABL are different during the daytime and nighttime. Indeed, recent findings by Xu et al. (2021) suggest that nocturnal BLH is mainly induced by intermittent turbulence (Shingleton, 2010), which is more related to SM rather than SH. Compared with the original series of BLH and meteorological variables, Pal and Haeffelin (2015) found correlations between BLH anomaly and variable anomalies over a single station were obviously reduced. Findings from our study indicated that global-scale correlations of anomalies for most variables are also weak (Fig. S11), with only WS and LTS anomalies maintaining a strong correlation; other variables were mainly independent of BLH long-term variation. As a sample, Fig. S12 provided the time series of anomalies at Camborne station (5.32°W, 50.22°N) and their correlation coefficients. Statistical results indicated that the LTS anomaly and WS anomaly are highly related with anomaly of BLH, and their correlations have obvious day-night difference. WS anomaly dominates the nighttime BLH anomaly but LTS anomaly the daytime. In recent decades, global WS has undergone drastic interannual and interdecadal variabilities (Zeng et al., 2019; Zhang and Wang, 2020), which are highly linked to the influences of weather processes and climate systems. Wang et al. (2019) revealed that detrended and de-seasonalized monthly WS anomalies in the

Fig. 4. Diurnal cycles of BLH under cloudy (left panel) and clear (right panel) cases. Only the land cover with more than 20 sounding stations is provided. Diurnal cycles are formed by converting UTC into the local sample time. The error bar represents the standard deviation, and X-axis is local time (hour), Y-axis is BLH (m).

Northern Hemisphere are dominated by general circulation, implying that the detrended BLH anomaly, especially the nocturnal BLH anomaly, is related to the anomaly of synoptic process. LTS denotes the potential temperature deference between 700 hPa and the surface, and a clear linear relationship exhibits between LTS and air temperature. The detrend temperature anomaly, however, filters out the effects of global warming, thus it still records large inter-annual fluctuations which are also influenced by general circulation (Wallace et al., 2012). Since surface temperature anomaly contributes are insignificant to the BLH anomaly, the anomaly of 700 hPa temperature may have an important influence on BLH anomalies.

3.3.2. Contribution to the BLH trend

Nearly 280 stations exhibited statistically significant annual linear trends. In order to examine causes for BLH trends, observed BLH and meteorological variables with significant annual trends were normalized and then stepwise regressed using Eq. (4), and contribution rates to trends of BLH anomaly (only de-seasonalized) were calculated as (Chen et al., 2020; Cheng et al., 2015):

$$C_i = \frac{\partial H/\partial x_i \cdot \Delta x_i}{\Delta H} \tag{6}$$

where, $\partial H/\partial x_i$ is the coefficient of stepwise regression; and ΔH (Δx_i) is the difference of average predicted BLH (meteorological factors) between the first and last ten years. Notably, derived contributions may include negative values and values >1. A negative contribution indicates that the variable trends inversely varied with the trend of BLH anomaly; a value >1 indicates that the strong contribution of the variable anomalies. In this study, we used the relative contribution rate calculated by absolute values, as per the method of Haji Gholizadeh et al. (2016):

$$C_{r,i} = \frac{|C_i|}{|C_1| + |C_2| + \cdots + |C_n|} \times 100\% \tag{7}$$

where, $C_{r,i}$ is the relative contribution of ith variable; $|C_i|$ is the absolute value of contribution calculated from Eq. (6); and n is the total number of variables in the regression model.

The global distributions of relative contribution rate of different factors to trends of BLH anomaly under clear sky conditions were shown in Fig. 6 (cloudy conditions see Fig. S13). In general, LTS and WS anomalies played important roles in determining trends of BLH anomaly, with LTS having a relatively greater contribution for the majority of stations. The contributions of RH and T notably increased, largely being caused by the effects of global warming. Other variables exhibited small contributions, even failing to enter the regression models. Global results also indicated that day-night differences in the contribution of WS were still significant evident. By grouping the contributions of T, RH, LTS and WS anomalies, we roughly assessed the diurnal cycle of averaged contributions (Fig. S14). Although WS was the dominating factor for BLH long-term variation, LTS trends had greater effects on predicted trends of BLH anomaly, especially for the clear-sky conditions. LTS contributed the most in the late afternoon, but a peak was also exhibited around 04:00 LT. As the source of this peak was mainly located at a station near 60°E (0000 UTC), an area noted for a poor regression performance (Fig. S15, failed correlation test), this peak was deemed to be noise. The contribution of WS during the daytime was distinctly lower than those of night; however, T and RH also had significant contributions in the morning.

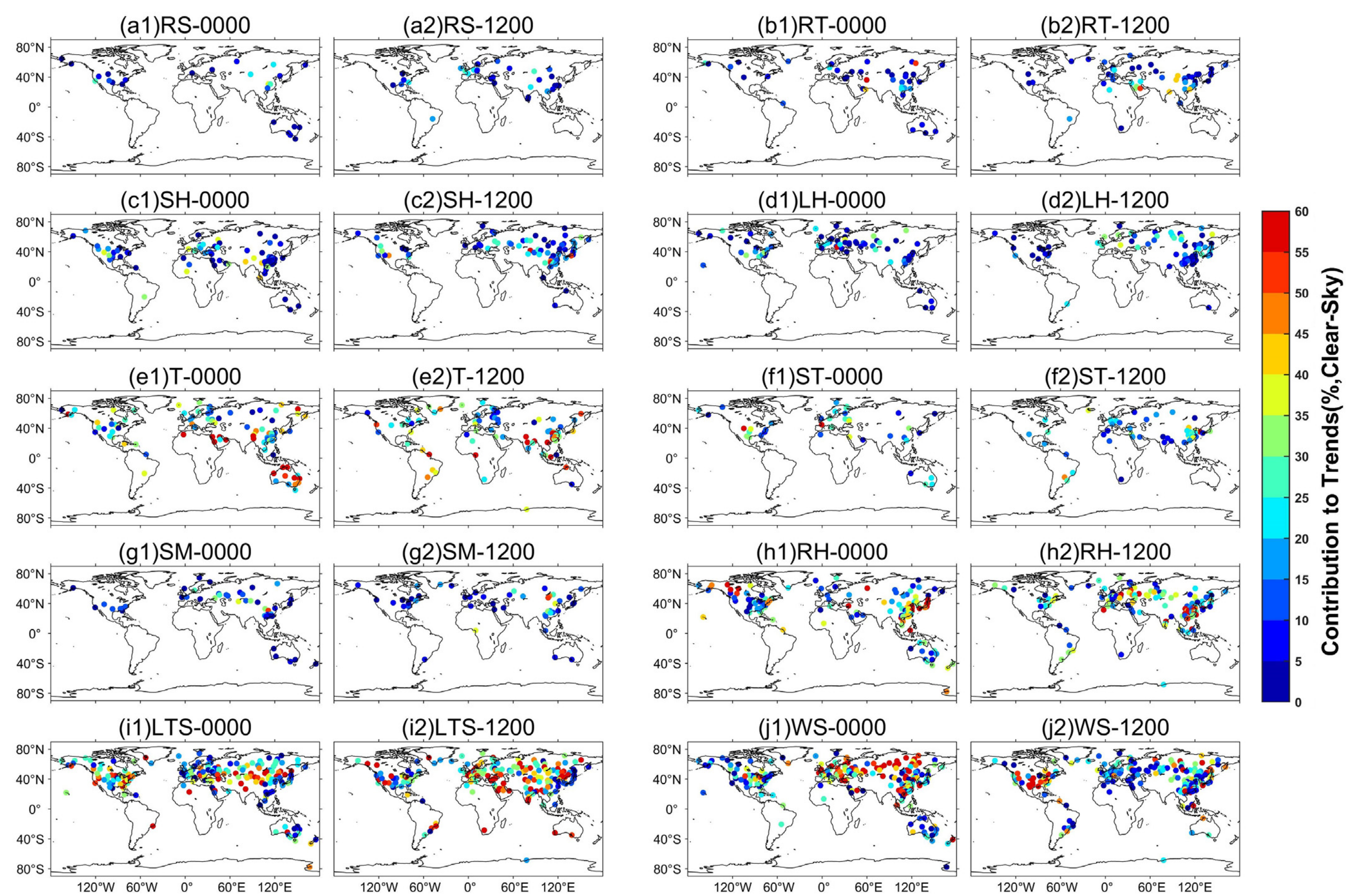

Fig. 6. Same to Fig. 5, but for the contribution from variable anomalies to the trend of BLH anomaly under clear-sky conditions; "0000" and "1200" denote UTC. The cloudy case is shown in Fig. S13.

Comparisons between observed (after de-seasonalizing) and predicted trends of BLH anomaly over eight land types (Fig. 7; left side of the dotted red line) clearly indicate that regression models capture the right sign of trends. As per results, all land types recorded mean increasing trends. Although regression results generally underestimated the trends, they captured BLH well (Fig. S15; Table S2) and were always within the uncertainty range of observed trends. The differences between observed and predicted trends may be due to the incomplete expression of a linear model, in fact, physical ABL processes could be complex and non-linear (Seidel et al., 2012). Moreover, regression

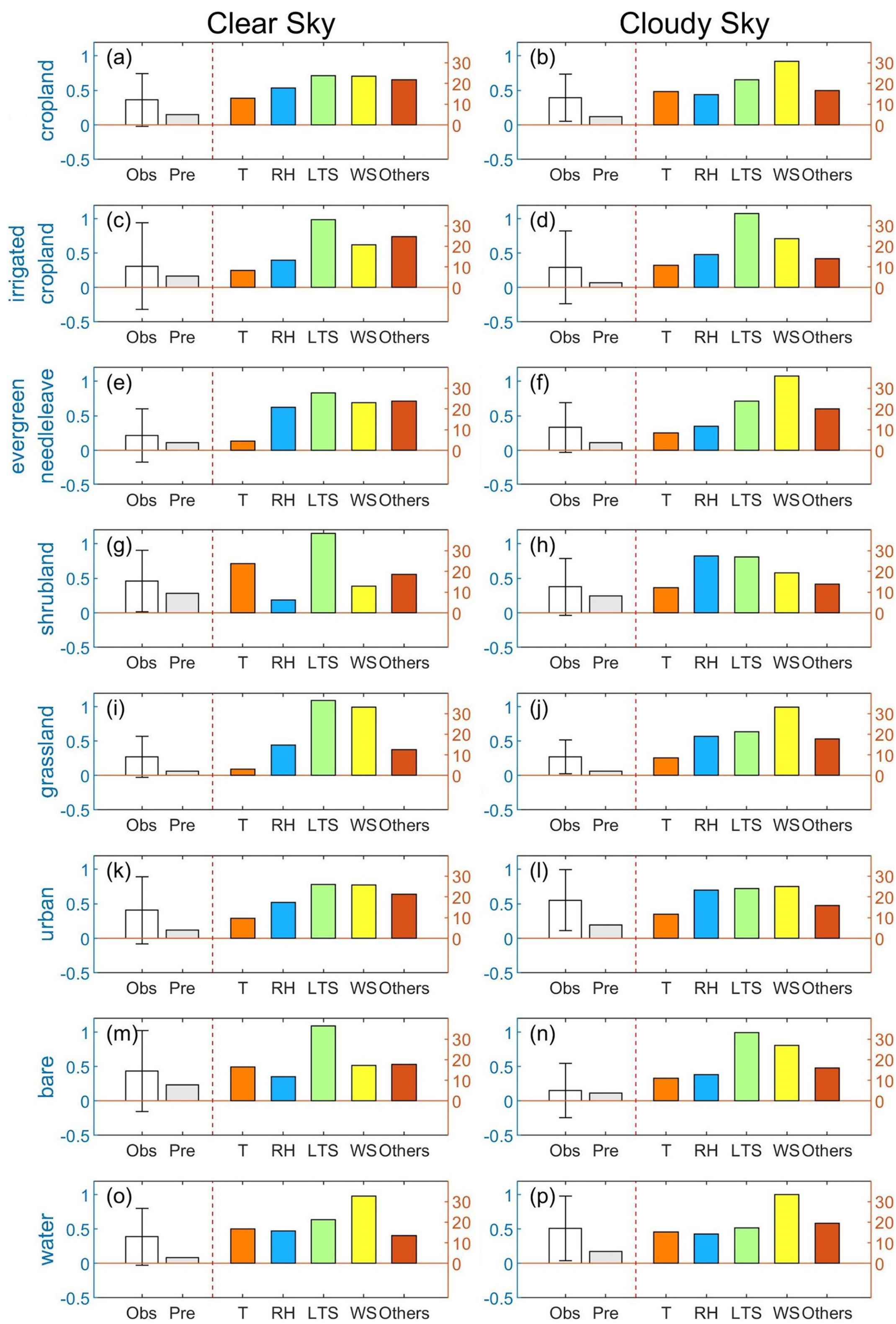

Fig. 7. Relative contributions (%) to predicted trends of BLH anomaly over eight land types are shown in right side of the dotted red dotted line, "Others" denotes the total contribution of variables in addition to T, RH, LTS, and WS. The left side of the dotted red line presents the observed BLH trends (Obs) and the regression models predicted trends (Pre) after normalization.

Table 1
Averaged contribution (%) to increased and decreased BLH trends from meteorological variables.

		T	RH	LTS	WS	Other
Clear-sky	Decrease	6.5	8.9	28.3	36.9	19.4
	Increase	13.8	19.2	28.5	19.7	18.8
Cloudy	Decrease	6.4	14.9	20.8	39.8	18.1
	Increase	14.5	20.8	24.9	23.7	16.1

models mainly consider variables related to surface forcing, but entrainment processes above ABL are also non-negligible (Angevine, 2007; Huang et al., 2020). However, it is difficult to quantify their contributions in the present study based on radiosonde observations; further analyses about entrainment in models will be undertaken in future work. The mean contributions from several main factors are shown on the right-hand side of the red dotted line in Fig. 7. LTS dominates predicted trends of BLH anomaly over most clear-sky land types (except water), as well as some cloud covered land (irrigated cropland, shrubland, bare land), and WS is generally the second most important factor.

Due to the generally decreasing trends in global land WS (Bichet et al., 2012; Torralba et al., 2017), the contribution of WS was obviously dominant for decreased BLH (Table 1). This presents a further interpretation for why decreased BLH mostly occurs during the nighttime, as WS plays more roles in nighttime ABL. A recent study suggested that decreased land WS is mainly caused by the increasing of surface friction (Wang et al., 2019), which may be strongly linked to global greening (Zhu et al., 2016) and urbanization (Li et al., 2017). T and RH are generally negatively correlated with each other, increases in T caused by global warming may also result in a decrease in RH. Both increased T and decreased RH (Fig. S16) can promote an increase in BLH, and they contributed more to increased BLH anomaly than that of decreased BLH anomaly. Although the LTS trend is a dominant factor for increasing the BLH trend, few studies, however, have focused on the LTS trend. Global warming has caused whole static stability increased (Frierson, 2006), however, LTS has declined over the past few decades because the 700 hPa warming is slower than the surface warming (Fig. S16), possibly being the main reason of decreasing trend of LTS. On the other hand, aerosols can affect the Earth energy balance (Che et al., 2019b), such as it causes the redistribution of energy by scattering and absorption, aerosol weakens solar energy during the day and indirectly weakens turbulent mixing; moreover, it warms the middle atmosphere and cools the surface, which in turn increases LTS (Malavelle et al., 2011). Most regions of the world exhibit negative trends in aerosol loading (Mortier et al., 2020) may weaken this effect, thereby reducing the LTS. The above four variables contributed the majority of predicted trends, with total contribution of other variables is below 20% from the perspective of global average. Clouds narrow the amplitude of annual BLH trends (Fig. S5; Table S1), clear-cloudy differences of BLH trends may be partly related to different degrees of contributions of variables. For example, contributions of LTS were weakened with the presence of clouds, while the contributions of WS and RH under cloudy conditions were larger. For the long-term variation and trend of BLH anomaly, contributions from T and RH are always larger in the tropics than the non-tropics, whereas the contribution of WS rapidly diminished; this indicates that the high temperature and high humidity meteorological conditions in the tropics have a greater influence on ABL (Table S3).

4. Conclusions

As a crucial parameter of ABL, BLH has important effects on the development and transport of pollutants, as well as weather and climate studies (Miao and Liu, 2019; Yim et al., 2019). Previous studies focused on retrieval methods and long-term trends of BLH, or its impact on dispersion of pollutants and aerosols. However, related studies about the attribution of its long-term variation (and trends) have received far less attention and are still poorly understood. In order to address this area of research, a long-term time series of BLH was calculated from a 39-years period of global sounding; contributions from meteorological factors to long-term variation and BLH trends were investigated. Although results from this study are in good agreement with those from previous investigations, some new insights are provided.

Multiple-year mean values indicated that BLHs at two fixed sampling times exhibit a regular latitudinal gradient due to inherent diurnal BLH cycles; boundary layer clouds reduce daytime thermal forcing and nighttime thermal loss (Huang et al., 2020), having opposite results in day-night BLH differences. More than 50% of the stations recorded statistically significant annual and seasonal trends, positive trends that were found on a global scale, and a few decreasing trends mainly existing at stations in the night. Seasonal trends were ordered as MAM > JJA > SON (or DJF), SON close to DJF.

Different characteristics in land cover, including soil moisture and thermal property, roughness, albedo and vegetation fraction (Ács et al., 2014; Burakowski et al., 2018) result in different BLH performances. Dry shrubland and bare land always recorded deeper BLH than water and irrigated cropland; evergreen needle-leaved land recorded relatively shallow BLH due to being located in high-latitude cool temperate zones. The dispersed distribution of urban stations resulted in an insignificant mean BLH, having the largest variation range. BLH diurnal cycles over eight lands had a general pattern with peaking in the later afternoon, highlighting significant differences between day and night, and between clear sky and cloudy conditions.

Stepwise regression models suitably captured the long-term variation and trends of BLH at most stations. The detrended WS and LTS anomalies indicated more influences than other factors from a long-term variation perspective, implying a possible linkage between detrended BLH anomaly and anomaly of general circulation. WS and LTS alternately dominated the diurnal anomaly in BLH, with LTS being the main contributor in the afternoon and WS at other periods. This result could be due to the day-night differences in the BLH forcing mechanism that are mainly determined by buoyancy flux and shear mechanical effects (Choi et al., 2011; Pino and Vilà-Guerau De Arellano, 2008). Non-detrended regression models generally underestimate BLH trends. Four variables (T, RH, WS and LTS) combined contributed to the majority of predicted annual BLH trends, contributions from T and RH to trend of BLH anomaly are larger than to long-term variation, due to the non-detrended anomalies contain the influences of global warming. Overall, LTS is the major contributor to trends of BLH anomaly and WS takes second place. LTS trend is determined by slower warming in 700 hPa than surface and possible decreasing of aerosol loading, as a result, global BLH has increased generally. In addition, due to global WS having undergone a significant decline in the last few decades (Torralba et al., 2017), WS also contributes nearly 40% of the decreased BLH anomaly. WS exhibits more influences on nocturnal BLH than daytime, such that the decreased BLH trends are mainly exhibited in night period.

In this work, global seasonal, diurnal and annual BLH characteristics were investigated, and contributions from surface parameters to BLH long-term variation and trend were quantified. However, this study lacks a detailed investigation on synoptic processes, aerosol loading etc., although these processes may be related to the BLH long-term variation and trend. Besides, the influences of cloud types and entrainment processes may also be the future research topics. Additionally, twice-daily radiosonde could not provide a complete diurnal cycle over a single station, the statistical diurnal cycle of BLH on a global or regional scale is still poorly understood and quantified. Space-born lidar, located on the non-sun-synchronous International Space Station (Matthew et al., 2015), may accumulate long-term datasets which may help to roughly obtain climatological diurnal variations of BLH over a certain region or globally. This is of great importance to BLH evolution and the mechanism studies on a daily scale, and to evaluate existing models.

CRediT authorship contribution statement

Yarong Li: Formal analysis, Data curation, Writing – original draft, Writing – review & editing. **Jiming Li:** Conceptualization, Methodology, Data curation, Writing – original draft, Writing – review & editing. **Yuxin Zhao:** Formal analysis, Data curation. **Miao Lei:** Formal analysis. **Yang Zhao:** Formal analysis. **Bida Jian:** Data curation, Writing – review & editing. **Min Zhang:** Formal analysis. **Jianping Huang:** Conceptualization, Methodology, Data curation, Writing – original draft, Writing – review & editing.

Declaration of competing interest

The authors declare that they have no known competing financial interests or personal relationships that could have appeared to influence the work reported in this paper.

Acknowledgments

This research was jointly supported by the Strategic Priority Research Program of the Chinese Academy of Sciences (XDA2006010301), the Innovative Research Groups of the National Science Foundation of China (41521004) and the National Science Fund for Excellent Young Scholars (42022037). The authors declare that they have no conflict of interest. We would like to thank the ERA5, ESA-CCI, C3S and University of Wyoming science teams for providing excellent and accessible data products that made this study possible.

Appendix A. Supplementary data

Supplementary data to this article can be found online at https://doi.org/10.1016/j.scitotenv.2021.148950.

References

Ács, F., Gyöngyösi, A.Z., Breuer, H., Horváth, Á., Mona, T., Rajkai, K., 2014. Sensitivity of WRF-simulated planetary boundary layer height to land cover and soil changes. Meteorol. Z. 23, 279–293. https://doi.org/10.1127/0941-2948/2014/0544.

Angevine, W.M., 2007. Transitional, entraining, cloudy, and coastal boundary layers. Acta Geophysica 56, 2–20. https://doi.org/10.2478/s11600-007-0035-1.

Banta, R.M., 2003. Mixing-height differences between land use types: dependence on wind speed. J. Geophys. Res. 108 (doi). https://doi.org/10.1029/2002jd002748.

Bianco, L., Djalalova, I.V., King, C.W., Wilczak, J.M., 2011. Diurnal evolution and annual variability of boundary-layer height and its correlation to other meteorological variables in California's Central Valley. Bound.-Layer Meteorol. 140, 491–511. https://doi.org/10.1007/s10546-011-9622-4.

Bichet, A., Wild, M., Folini, D., Schär, C., 2012. Causes for decadal variations of wind speed over land: sensitivity studies with a global climate model. Geophys. Res. Lett. 39. https://doi.org/10.1029/2012gl051685 (n/a-n/a).

Blay-Carreras, E., et al., 2014. Role of the residual layer and large-scale subsidence on the development and evolution of the convective boundary layer. Atmos. Chem. Phys. 14, 4515–4530. https://doi.org/10.5194/acp-14-4515-2014.

Burakowski, E., et al., 2018. The role of surface roughness, albedo, and Bowen ratio on ecosystem energy balance in the Eastern United States. Agric. For. Meteorol. 249, 367–376. https://doi.org/10.1016/j.agrformet.2017.11.030.

Che, H., et al., 2019a. Large contribution of meteorological factors to inter-decadal changes in regional aerosol optical depth. Atmos. Chem. Phys. 19, 10497–10523. https://doi.org/10.5194/acp-19-10497-2019.

Che, H., et al., 2019b. Spatial distribution of aerosol microphysical and optical properties and direct radiative effect from the China Aerosol Remote Sensing Network. Atmos. Chem. Phys. 19, 11843–11864. https://doi.org/10.5194/acp-19-11843-2019.

Chen, L., Zhu, J., Liao, H., Yang, Y., Yue, X., 2020. Meteorological influences on PM2.5 and O3 trends and associated health burden since China's clean air actions. Sci. Total Environ. 744, 140837. https://doi.org/10.1016/j.scitotenv.2020.140837.

Cheng, S., Guan, X., Huang, J., Ji, F., Guo, R., 2015. Long-term trend and variability of soil moisture over East Asia. J. Geophys. Res. Atmos. 120, 8658–8670. https://doi.org/10.1002/2015jd023206.

Choi, W., Faloona, I.C., McKay, M., Goldstein, A.H., Baker, B., 2011. Estimating the atmospheric boundary layer height over sloped, forested terrain from surface spectral analysis during BEARPEX. Atmos. Chem. Phys. 11, 6837–6853. https://doi.org/10.5194/acp-11-6837-2011.

Davy, R., Esau, I., 2016. Differences in the efficacy of climate forcings explained by variations in atmospheric boundary layer depth. Nat. Commun. 7, 11690. https://doi.org/10.1038/ncomms11690.

Ding, A., Huang, X., Fu, C., 2017. Air Pollution and Weather Interaction in East Asia. Oxford University Press https://doi.org/10.1093/acrefore/9780199389414.013.536.

Durre, I., Vose, R.S., Wuertz, D.B., 2006. Overview of the integrated global radiosonde archive. J. Clim. 19, 53–68. https://doi.org/10.1175/JCLI3594.1.

Endo, S., Shinoda, T., Hiyama, T., Uyeda, H., Nakamura, K., Tanaka, H., Tsuboki, K., 2008. Characteristics of vertical circulation in the convective boundary layer over the Huaihe River Basin in China in the early summer of 2004. J. Appl. Meteorol. Climatol. 47, 2911–2928. https://doi.org/10.1175/2008jamc1769.1.

Fekih, A., Mohamed, A., 2019. Evaluation of the WRF model on simulating the vertical structure and diurnal cycle of the atmospheric boundary layer over Bordj Badji Mokhtar (southwestern Algeria). J. King Saud Univ. Sci. 31, 602–611. https://doi.org/10.1016/j.jksus.2017.12.004.

Friedl, M.A., Sulla-Menashe, D., Tan, B., Schneider, A., Ramankutty, N., Sibley, A., Huang, X., 2010. MODIS Collection 5 global land cover: algorithm refinements and characterization of new datasets. Remote Sens. Environ. 114, 168–182. https://doi.org/10.1016/j.rse.2009.08.016.

Frierson, D.M.W., 2006. Robust increases in midlatitude static stability in simulations of global warming. Geophys. Res. Lett. 33. https://doi.org/10.1029/2006gl027504.

Garratt, J.R., 1994. The atmospheric boundary-layer - review. Earth-Sci. Rev. 37, 89–134. https://doi.org/10.1016/0012-8252(94)90026-4.

Guo, J., et al., 2016. The climatology of planetary boundary layer height in China derived from radiosonde and reanalysis data. Atmos. Chem. Phys. 16, 13309–13319. https://doi.org/10.5194/acp-16-13309-2016.

Guo, J., et al., 2019. Shift in the temporal trend of boundary layer height in China using long-term (1979–2016) radiosonde data. Geophys. Res. Lett. 46, 6080–6089. https://doi.org/10.1029/2019gl082666.

Haji Gholizadeh, M., Melesse, A.M., Reddi, L., 2016. Water quality assessment and apportionment of pollution sources using APCS-MLR and PMF receptor modeling techniques in three major rivers of South Florida. Sci. Total Environ. 566–567, 1552–1567. https://doi.org/10.1016/j.scitotenv.2016.06.046.

Harrison, E.F., Minnis, P., Barkstrom, B.R., Ramanathan, V., Cess, R.D., Gibson, G.G., 1990. Seasonal variation of cloud radiative forcing derived from the Earth Radiation Budget Experiment. J. Geophys. Res. 95, 18687–18703. https://doi.org/10.1029/JD095iD11p18687.

Hu, X.M., et al., 2014. Impact of the Loess Plateau on the atmospheric boundary layer structure and air quality in the North China Plain: a case study. Sci. Total Environ. 499, 228–237. https://doi.org/10.1016/j.scitotenv.2014.08.053.

Huang, J., Yi, Y., 1991. Inversion of a nonlinear dynamical model from the observation. J. Sci. China Ser. B 1246–1251.

Huang, Q.Q., Cai, X.H., Song, Y., 2016. A numerical study of sea breeze and spatiotemporal variation in the coastal atmospheric boundary layer at Hainan Island, China. Boundary Layer Meteorol. 161, 543–560. https://doi.org/10.1007/s10546-016-0177-2.

Huang, X., Ding, A., Wang, Z., Ding, K., Gao, J., Chai, F., Fu, C., 2020. Amplified transboundary transport of haze by aerosol–boundary layer interaction in China. Nat. Geosci. 13, 428–434. https://doi.org/10.1038/s41561-020-0583-4.

Jian, B., Li, J., Wang, G., He, Y., Han, Y., Zhang, M., Huang, J., 2018. The impacts of atmospheric and surface parameters on long-term variations in the planetary albedo. J. Clim. 31, 8705–8718. https://doi.org/10.1175/jcli-d-17-0848.1.

Kendall, M.G., 1975. Rank Correlation Methods. Charles Griffin, London, UK.

Kim, S.-W., Yoon, S.-C., Won, J.-G., Choi, S.-C., 2007. Ground-based remote sensing measurements of aerosol and ozone in an urban area: a case study of mixing height evolution and its effect on ground-level ozone concentrations. Atmos. Environ. 41, 7069–7081. https://doi.org/10.1016/j.atmosenv.2007.04.063.

Lanzante, J.R., 1996. Resistant, robust and non-parametric techniques for the analysis of climate data: theory and examples, including applications to historical radiosonde station data. Int. J. Climatol. 16, 1197–1226. https://doi.org/10.1002/(SICI)1097-0088(199611)16:11<1197::AID-JOC89>3.0.CO;2-L.

Leventidou, E., Zanis, P., Balis, D., Giannakaki, E., Pytharoulis, I., Amiridis, V., 2013. Factors affecting the comparisons of planetary boundary layer height retrievals from CALIPSO, ECMWF and radiosondes over Thessaloniki, Greece. Atmos. Environ. 74, 360–366. https://doi.org/10.1016/j.atmosenv.2013.04.007.

Li, Z., Song, L., Ma, H., Xiao, J., Wang, K., Chen, L., 2017. Observed surface wind speed declining induced by urbanization in East China. Clim. Dyn. 50, 735–749. https://doi.org/10.1007/s00382-017-3637-6.

Liang, X.-Z., Liu, S., 2010. Observed diurnal cycle climatology of planetary boundary layer height. J. Clim. 23, 5790–5809. https://doi.org/10.1175/2010jcli3552.1.

Malavelle, F., Pont, V., Mallet, M., Solmon, F., Johnson, B., Leon, J.-F., Liousse, C., 2011. Simulation of aerosol radiative effects over West Africa during DABEX and AMMA SOP-0. J. Geophys. Res. 116. https://doi.org/10.1029/2010jd014829.

Mann, H.B., 1945. Nonparametric tests against trend. Econometrica 13, 245–259. https://doi.org/10.2307/1907187.

Matthew, J.M., John, E.Y., Scott, V.S., Andrew, W.K., Patrick, A.S., 2015. The Cloud-Aerosol Transport System (CATS): a technology demonstration on the International Space Station. Proc. SPIE https://doi.org/10.1002/2016jd025937.

Medeiros, B., Deser, C., Tomas, R.A., Kay, J.E., 2011. Arctic inversion strength in climate models. J. Clim. 24, 4733–4740. https://doi.org/10.1175/2011jcli3968.1.

Meng, X., et al., 2017. Detecting hydrological consistency between soil moisture and precipitation and changes of soil moisture in summer over the Tibetan Plateau. Clim. Dyn. 51, 4157–4168. https://doi.org/10.1007/s00382-017-3646-5.

Miao, Y., Liu, S., 2019. Linkages between aerosol pollution and planetary boundary layer structure in China. Sci. Total Environ. 650, 288–296. https://doi.org/10.1016/j.scitotenv.2018.09.032.

Miao, Y., Che, H., Zhang, X., Liu, S., 2021. Relationship between summertime concurring PM2.5 and O3 pollution and boundary layer height differs between Beijing and Shanghai, China. Environ. Pollut. 268, 115775. https://doi.org/10.1016/j.envpol.2020.115775.

Molod, A., Salmun, H., Dempsey, M., 2015. Estimating planetary boundary layer heights from NOAA profiler network wind profiler data. J. Atmos. Ocean. Technol. 32, 1545–1561. https://doi.org/10.1175/jtech-d-14-00155.1.

Mortier, A., et al., 2020. Evaluation of climate model aerosol trends with ground-based observations over the last 2 decades – an AeroCom and CMIP6 analysis. Atmos. Chem. Phys. 20, 13355–13378. https://doi.org/10.5194/acp-20-13355-2020.

Pal, S., Haeffelin, M., 2015. Forcing mechanisms governing diurnal, seasonal, and interannual variability in the boundary layer depths: five years of continuous lidar observations over a suburban site near Paris. J. Geophys. Res. Atmos. 120. https://doi.org/10.1002/2015jd023268.

Pal, S., et al., 2012. Spatio-temporal variability of the atmospheric boundary layer depth over the Paris agglomeration: an assessment of the impact of the urban heat island intensity. Atmos. Environ. 63, 261–275. https://doi.org/10.1016/j.atmosenv.2012.09.046.

Pielke, R.A., 2001. Influence of the spatial distribution of vegetation and soils on the prediction of cumulus convective rainfall. Rev. Geophys. 39, 151–177. https://doi.org/10.1029/1999rg000072.

Pino, D., Vilà-Guerau De Arellano, J., 2008. Effects of shear in the convective boundary layer: analysis of the turbulent kinetic energy budget. Acta Geophys. 56, 167–193. https://doi.org/10.2478/s11600-007-0037-z.

Poore, K.D., Wang, J., Rossow, W.B., 1995. Cloud layer thicknesses from a combination of surface and upper-air observations. J. Clim. 8, 550–568. https://doi.org/10.1175/1520-0442(1995)008<0550:CLTFAC>2.0.CO;2.

Raffalovich, L.E., 1994. Detrending time series: a cautionary note. Sociol. Methods Res. 22, 492–519. https://doi.org/10.1177/0049124194022004003.

Rummukainen, M., 2013. Climate change: changing means and changing extremes. Clim. Chang. 121, 3–13. https://doi.org/10.1007/s10584-013-0888-z.

Sanchez-Mejia, Z.M., Papuga, S.A., 2014. Observations of a two-layer soil moisture influence on surface energy dynamics and planetary boundary layer characteristics in a semiarid shrubland. Water Resour. Res. 50, 306–317. https://doi.org/10.1002/2013wr014135.

Seibert, P., Beyrich, F., Gryning, S.-E., Joffre, S., Rasmussen, A., Tercier, P., 2000. Review and intercomparison of operational methods for the determination of the mixing height. Atmos. Environ. 34, 1001–1027. https://doi.org/10.1016/S1352-2310(99)00349-0.

Seidel, D.J., Ao, C.O., Li, K., 2010. Estimating climatological planetary boundary layer heights from radiosonde observations: comparison of methods and uncertainty analysis. J. Geophys. Res. 115. https://doi.org/10.1029/2009jd013680.

Seidel, D.J., Zhang, Y., Beljaars, A., Golaz, J.-C., Jacobson, A.R., Medeiros, B., 2012. Climatology of the planetary boundary layer over the continental United States and Europe. J. Geophys. Res. Atmos. 117. https://doi.org/10.1029/2012jd018143 (n/a-n/a).

Sen, P.K., 1968. Estimates of the regression coefficient based on Kendall's Tau. J. Am. Stat. Assoc. 63, 1379–1389. https://doi.org/10.1080/01621459.1968.10480934.

Shingleton, N., 2010. Coupling a Land-surface Model to Large-eddy Simulation to Study the Nocturnal Boundary Layer. The University of Utah.

Stull, R.B., 1988. An Introduction to Boundary Layer Meteorology. Kluwer Academic (666 pp.).

Tanaka, H., et al., 2007. Surface flux and atmospheric boundary layer observations from the LAPS project over the middle stream of the Huaihe River basin in China. Hydrol. Process. 21, 1997–2008. https://doi.org/10.1002/hyp.6706.

Torralba, V., Doblas-Reyes, F.J., Gonzalez-Reviriego, N., 2017. Uncertainty in recent near-surface wind speed trends: a global reanalysis intercomparison. Environ. Res. Lett. 12. https://doi.org/10.1088/1748-9326/aa8a58.

Vogelezang, D.H.P., Holtslag, A.A.M., 1996. Evaluation and model impacts of alternative boundary-layer height formulations. Bound.-Layer Meteorol. 81, 245–269. https://doi.org/10.1007/BF02430331.

Wallace, J.M., Fu, Q., Smoliak, B.V., Lin, P., Johanson, C.M., 2012. Simulated versus observed patterns of warming over the extratropical Northern Hemisphere continents during the cold season. Proc. Natl. Acad. Sci. U. S. A. 109, 14337–14342. https://doi.org/10.1073/pnas.1204875109.

Wang, X.Y., Wang, K.C., 2014. Estimation of atmospheric mixing layer height from radiosonde data. Atmos. Meas. Tech. 7, 1701–1709. https://doi.org/10.5194/amt-7-1701-2014.

Wang, X., Wang, K., 2016. Homogenized variability of radiosonde-derived atmospheric boundary layer height over the global land surface from 1973 to 2014. J. Clim. 29, 6893–6908. https://doi.org/10.1175/jcli-d-15-0766.1.

Wang, K., Zhang, Z., Chen, D., Li, J., Dickinson, R., 2019. Increase in surface friction dominates the observed surface wind speed decline during 1973–2014 in the northern hemisphere lands. J. Clim. 32, 7421–7435. https://doi.org/10.1175/jcli-d-18-0691.1.

Wever, N., 2012. Quantifying trends in surface roughness and the effect on surface wind speed observations. J. Geophys. Res. Atmos. 117. https://doi.org/10.1029/2011jd017118 (n/a-n/a).

White, J.M., Eaton, F.D., Auer, A.H., 1978. The net radiation budget of the St. Louis metropolitan area. J. Appl. Meteorol. Climatol. 17, 593–599. https://doi.org/10.1175/1520-0450(1978)017<0593:TNRBOT>2.0.CO;2.

Wyant, M.C., Wood, R., Bretherton, C.S., Mechoso, C.R., Bacmeister, J., Balmaseda, M.A., Barrett, B., Codron, F., Earnshaw, P., Fast, J., Hannay, C., Kaiser, J.W., Kitagawa, H., Klein, S.A., Köhler, M., Manganello, J., Pan, H.-L., Sun, F., Wang, S., Wang, Y., 2010. The PreVOCA experiment: modeling the lower troposphere in the Southeast Pacific. Atmos. Chem. Phys. 10, 4757–4774. https://doi.org/10.5194/acp-10-4757-2010.

Xiao, B., Bowker, M.A., 2020. Moss-biocrusts strongly decrease soil surface albedo, altering land-surface energy balance in a dryland ecosystem. Sci. Total Environ. 741, 140425. https://doi.org/10.1016/j.scitotenv.2020.140425.

Xu, Z., Chen, H., Guo, J., Zhang, W., 2021. Contrasting effect of soil moisture on the daytime boundary layer under different thermodynamic conditions in summer over China. Geophys. Res. Lett. 48. https://doi.org/10.1029/2020gl090989.

Yi, C., Davis, K.J., Berger, B.W., Bakwin, P.S., 2001. Long-term observations of the dynamics of the continental planetary boundary layer. J. Atmos. Sci., 58, 1288–1299 https://doi.org/10.1175/1520-0469(2001)058<1288:LTOOTD>2.0.CO;2.

Yim, S.H.L., Hou, X., Guo, J., Yang, Y., 2019. Contribution of local emissions and transboundary air pollution to air quality in Hong Kong during El Niño-Southern Oscillation and heatwaves. Atmos. Res. 218, 50–58. https://doi.org/10.1016/j.atmosres.2018.10.021.

Zeng, Z., et al., 2019. A reversal in global terrestrial stilling and its implications for wind energy production. Nat. Clim. Chang. 9, 979–985. https://doi.org/10.1038/s41558-019-0622-6.

Zhang, Y., Li, S., 2019. Climatological characteristics of planetary boundary layer height over Japan. Int. J. Climatol. 39, 4015–4028. https://doi.org/10.1002/joc.6056.

Zhang, Y., Seidel, D.J., 2011. Challenges in estimating trends in Arctic surface-based inversions from radiosonde data. Geophys. Res. Lett. 38. https://doi.org/10.1029/2011gl048728 (n/a-n/a).

Zhang, Z., Wang, K., 2020. Stilling and recovery of the surface wind speed based on observation, reanalysis, and geostrophic wind theory over China from 1960 to 2017. J. Clim. 33, 3989–4008. https://doi.org/10.1175/jcli-d-19-0281.1.

Zhang, D., Iwasaka, Y., Matsuki, A., Ueno, K., Matsuzaki, T., 2006. Coarse and accumulation mode particles associated with Asian dust in southwestern Japan. Atmos. Environ. 40, 1205–1215. https://doi.org/10.1016/j.atmosenv.2005.10.037.

Zhang, D., Chen, B., Yamada, M., Niu, H., Wang, B., Iwasaka, Y., Shi, G., 2012. Elevated soot layer in polluted urban atmosphere: a case study in Beijing. J. Meteorol. Soc. Japan Ser. II 90, 361–375. https://doi.org/10.2151/jmsj.2012-302.

Zhang, Y., Seidel, D.J., Zhang, S., 2013. Trends in planetary boundary layer height over Europe. J. Clim. 26, 10071–10076. https://doi.org/10.1175/jcli-d-13-00108.1.

Zhang, W., et al., 2018. On the summertime planetary boundary layer with different thermodynamic stability in China: a radiosonde perspective. J. Clim. 31, 1451–1465. https://doi.org/10.1175/jcli-d-17-0231.1.

Zhang, H., et al., 2020. Research progress on estimation of the atmospheric boundary layer height. J. Meteorol. Res. 34, 482–498. https://doi.org/10.1007/s13351-020-9910-3.

Zhao, H., et al., 2019. Climatology of mixing layer height in China based on multi-year meteorological data from 2000 to 2013. Atmos. Environ. 213, 90–103. https://doi.org/10.1016/j.atmosenv.2019.05.047.

Zhu, Z.C., et al., 2016. Greening of the Earth and its drivers. Nat. Clim. Chang. 6, 791–795. https://doi.org/10.1038/nclimate3004.